

Electron acceleration by cascading reconnection in the solar corona

I Magnetic gradient and curvature effects

X. Zhou^{1,2}, J. Büchner¹, M. Bárta^{1,3}, W. Gan², and S. Liu²

¹ Max Planck Institute for Solar System Research, Justus-von-Liebig-Weg 3, 37077 Göttingen
e-mail: zhou@mps.mpg.de

² Key Laboratory of Dark Matter and Space Astronomy, Purple Mountain Observatory, Chinese Academy of Sciences, Nanjing, 210008, China

³ Astronomical Institute of Czech Academy of Sciences, Ondřejov, Czech Republic

ABSTRACT

Aims. We investigate the electron acceleration in convective electric fields of cascading magnetic reconnection in a flaring solar corona and show the resulting hard X-ray (HXR) radiation spectra caused by Bremsstrahlung for the coronal source.

Methods. We perform test particle calculation of electron motions in the framework of a guiding center approximation. The electromagnetic fields and their derivatives along electron trajectories are obtained by linearly interpolating the results of high-resolution adaptive mesh refinement (AMR) MHD simulations of cascading magnetic reconnection. Hard X-ray (HXR) spectra are calculated using an optically thin Bremsstrahlung model.

Results. Magnetic gradients and curvatures in cascading reconnection current sheet accelerate electrons: trapped in magnetic islands, precipitating to the chromosphere and ejected into the interplanetary space. The final location of an electron is determined by its initial position, pitch angle and velocity. These initial conditions also influence electron acceleration efficiency. Most of electrons have enhanced perpendicular energy. Magnetic curvature and gradient driven acceleration efficiency along the magnetic field increases with the increase of the magnetic field resolution. It was shown that for a sufficiently high resolution of the electromagnetic fields, adaptive mesh refinement (AMR) MHD simulations are needed. Trapped electrons can be accelerated to energies up to half of MeV , precipitating ones to more than $60 keV$ in the refined smaller-scale magnetic structures. Trapped electrons are considered to cause the observed bright spots along coronal mass ejection CME-trailing current sheets as well as the flare loop-top HXR emissions. Another observable effect is the locations of the precipitating energetic electrons with respect to the polarity inversion line (PIL). A stronger asymmetry of the energetic electron precipita-

tions around the PIL is obtained with sufficiently well resolved smaller-scale magnetic structures than that in the coarsely resolved ones due to the asymmetry in the parallel magnetic curvature acceleration.

Key words. Solar flare electron acceleration – Adiabatic acceleration – Hard X-ray – UV radiation
– Cascading reconnection

1. Introduction

Since the first recorded white light observations of solar flares (Carrington 1859; Hodgson 1859), sophisticated ground-based and space-born solar techniques have been introduced to investigate the physics of the sun. Recently space telescopes like SoHO, Yokoh, RHESSI, Hinode and SDO, have revealed many detailed observations covering broad wavelength ranges at a high temporal, spatial and spectral resolution.

Generally, it is accepted that the energy of solar flares comes from stressed, non-potential, current-carrying coronal magnetic fields being released by magnetic reconnection. About 10 to 50% of the flare energy may be transferred to energetic electrons and ions (e.g. Lin & Hudson 1976). In some cases energetic electrons alone carried away 50% of the flare energy (e.g. Miller et al. 1997), being accelerated to energies up to 10 – 100 *MeV* (e.g. Aschwanden 2002).

The prime diagnostic of accelerated electrons in solar flares is the HXR radiation they cause. Two main components were identified in HXR light curves : a sharply increasing component and a slowly varying one. The sharp increase happens within 0.5-5 s after the initial flaring (e.g. Holman et al. 2011; Zharkova et al. 2011). This indicates that within sub-second electrons are locally accelerated in excess of a few *MeV*. The slowly varying component lasts as long as flares continue, i.e., electron energization continues.

Using high-resolution imaging, HXR location in the sun has been solved with a few arcseconds resolution. Solar observations have shown HXR emissions from the foot-points of flaring coronal structures. Recently based on the classical CSHKP (see Priest & Forbes 2002 for a review) solar flare reconnection model and solar flare observations near the limb of the solar disk, HXRs were found also at the flare loop tops (e.g., Masuda et al. 1994; Gordovskyy et al. 2010b with Yokoh observation).

Although a substantial progress was made in observations, it is still an open question by which mechanisms the flare electrons are accelerated. Mostly suggested mechanisms can be divided into three classes (1) acceleration by direct current (DC) electric fields (see, e.g., Zharkova & Gordovskyy 2004, 2005a,b), (2) stochastic acceleration (see, e.g., Vlahos & Cargill 2009) and (3) shock acceleration (see, e.g., Aschwanden 2002; Benz 2008). Observations show also that different flares produce different HXR spectra changing with time and their locations with respect to the polarity inversion line (PIL) (e.g., Zharkova et al. 2011). All these features can hardly be

explained by one single acceleration mechanism. Therefore flare energetic particles are perhaps accelerated by different mechanisms at different time and in different places while the flares last.

In order to validate acceleration mechanism, it is appropriate to carry out test particle calculations. The electron acceleration in the vicinity of a single reconnection X-point, e.g., was investigated by Zharkova & Gordovskyy 2004, 2005a,b; Wood & Neukirch 2005; Priest & Titov 1996). Analytic reconnection models were used as well as the results of ideal or resistive MHD numerical simulations. Martens & Young 1990, e.g., used MHD simulation results to study the particle motions and accelerations in current sheets. In all these models the magnetic field parallel component of the DC electric field $\mathbf{E} = -\mathbf{u} \times \mathbf{B} + \eta \mathbf{J}$ causes strong particle acceleration if only η was chosen appropriately. However, the prescription of η in the resistive MHD simulations is usually ad hoc and arbitrary. Meanwhile in the collisionless corona, the concept of collisional resistivity η is largely unapplicable. Microphysical effects have to be taken into account. Silin et al. 2005; Büchner & Elkina 2006, e.g., have shown that considering possible micro-turbulence strong parallel electric fields must be confined in narrow channels of the ion inertia scale size (see also J. Büchner and W. Daughton 2007, section 3.5 in Birn & Priest (2007)). Macroscopic MHD simulations, on the other hand, is better to be used to investigate the electron acceleration in the convective electric fields ($\mathbf{E} = -\mathbf{u} \times \mathbf{B}$). Vekstein & Browning 1997 and Guo et al. 2010, e.g., analysed the particle acceleration in the convective electric fields around and at a magnetic null point, respectively.

Vekstein & Browning 1997 used an analytically prescribed magnetic field with an added uniform electric field in the perpendicular direction to calculate the test particle guiding center motions near a reconnection X-point in a 2D geometry. They restricted the test particle orbits far away from the X-point since the guiding center approximation breaks down in a null-point. They considered particle parallel acceleration due to the $\mathbf{E} \times \mathbf{B}$ drift effects and neglected the effects of magnetic gradients and curvatures by launching only particles with very small initial parallel velocities and magnetic moments. As other authors before (e.g., Burkhart et al. 1990), they found the final kinetic energy of the most accelerated particle is proportional to $E^{4/3}$, where $E = -\mathbf{u} \times \mathbf{B}$. They also assessed the spectral index of the accelerated particles as being about 1.7, the corresponding HXR spectral index would be around 2.7 utilizing a simple relation $\gamma_s = \delta + 1$ (where δ is the electron spectral index and γ_s stands for the index of emitted HXR spectrum) which is valid within the thin target model (Datlowe & Lin 1973).

Contrary to Vekstein & Browning 1997, Guo et al. 2010 took the output of a 3D MHD simulation of magnetic null point reconnection to study the electron and proton acceleration at a 3D null point in the convective electric field. Every test particle is traced by solving the full equations of motion. This is necessary since the guiding center approximation breaks down at a magnetic null point. They investigated the influence of the convective speed on particle acceleration by rescaling it. They found that all particles are more efficiently accelerated with a larger convective speed. Particle energy can be up to energies of the order of 2 MeV (proton) and 3 keV (electron) from initial thermal energy of about 200 eV. The reason is that non-adiabatic (demagnetized) particles

can easily be accelerated in the direction perpendicular to the magnetic field. Particles have to undergo strong perpendicular drift to be substantially accelerated. But particle final parallel energy can still dominate its final total kinetic energy. Because of the much smaller gyroradius, electrons are demagnetized in smaller regions than the protons, protons are accelerated to higher energies than electrons. These authors also studied the influence of the initial energy on particle acceleration: higher initial energies lead protons to be stronger accelerated, while the final kinetic energy of electrons were not influenced essentially.

In the studies of Vekstein & Browning 1997 and Guo et al. 2010, there were only one magnetic X- or null point. Krucker et al. 2008 claimed that electron DC-acceleration at only one reconnection X-point (e.g., Zharkova & Gordovskyy 2005a; Wood & Neukirch 2005) cannot explain the huge number of accelerated electrons inferred from HXR observations. The possibility of particle acceleration by cascading reconnection was mentioned firstly by Shibata & Tanuma 2001. They conjectured that magnetic islands could be formed at many scales by tearing-mode instabilities of the stretching current sheet. Later this concept are confirmed by theoretical approaches (e.g., Loureiro et al. 2007; Uzdensky et al. 2010), observations (e.g., Hoshino et al. 1994; Karlický 2004), AMR MHD simulations (e.g., Bárta et al. 2011) and particle in cell (PIC) simulations (e.g., Karlický et al. 2012). The electron acceleration by many reconnection sites was studied by Li & Lin 2012 and Gordovskyy et al. 2010a,b. In their studies, however, they assumed arbitrary ad-hoc prescribed anomalous resistivity models to reveal the accelerating fields. As well as the number of X-points in their studies were obtained by periodically repeating the simulation domain.

Only the particle acceleration in the convective electric fields $\mathbf{E} = -\mathbf{u} \times \mathbf{B}$, however, is independent on any ad hoc assumption about anomalous resistivity. In order to understand its possible acceleration effects, we use the results of AMR-MHD simulations of multiple island formations by cascading reconnection (Bárta et al. 2010, 2011). Those simulations have shown that cascading reconnection forms differently sized magnetic islands where electrons can be accelerated (see Sect.2). We use two different magnetic structure resolutions to investigate the resolution influence on electron accelerations. We studied the electron acceleration by cascading reconnection not only near the X-points but also in the magnetic islands in the framework of a guiding center approximation (Northrop 1963, see Sect.3). The resulting HXR emissions by energetic electron non-thermal Bremsstrahlung are derived using an optically thin Bremsstrahlung method (Brown 1971; Tandberg-Hanssen & Emslie 1988) to compare with flare HXR observations. In Sect.4, electron acceleration dependence on initial conditions, different acceleration factors in the parallel direction, acceleration in different (parallel and perpendicular) direction, as well as trajectories, are investigated for trapped (Sect.4.1) and precipitating (Sect.4.2) electrons. Finally the results are discussed and conclusion are drawn in Sect.5.

2. Electromagnetic fields of cascading reconnection

In this study we aim to investigate the particle acceleration in the convective electric fields of differently resolved cascading reconnection current sheets trailing a flaring arcade behind an ejected flux rope (cf. Lin & Forbes 2000).

The fields of cascading magnetic reconnection are obtained by means of a 2.5D AMR MHD simulation (Bárta et al. 2010, 2011). In traditional MHD simulations, there are only uniform grid points. Unfortunately the sub-grid physics become important when the current sheet width and the non-idea plasma domain become thinner than the numerical grid size. Hence, traditional coarse MHD simulation cannot study smaller-scale processes of anticipated cascading reconnection. In order to resolve smaller-scale magnetic structures in the thinner current sheets, we use simulation results which can cover an as large as possible scale range. The high resolution AMR MHD technique allows the description of smaller-scale magnetic structures. For that sake the refined mesh is used when the current sheet width becomes comparable with the initial coarse grid size.

The AMR algorithm works as follows: If at the time-step $t + \Delta t$ some coarse grids are detected containing thin current sheet, then they will locally be split into sub-boxes with 10×10 grid-points in the sub-system. After such refined meshes are initialized, the necessary more detailed plasma and field values are obtained by interpolating their parent coarse system values at the last time step (t). Then the dynamics of both the newly created and the pre-existing refined meshes are evolved in time ($t \rightarrow t + \Delta t$) with an accordingly refined time-step. After that the plasma and field values at the parent coarse mesh are replaced by averaging the quantities obtained from its corresponding refined meshes at time-step $t + \Delta t$. The influence of the global dynamics on the refined meshes are considered by interpolating boundary conditions in time and space. This refinement is repeated until the whole simulation is over (see Bárta et al. 2010).

So there are two sets of electromagnetic field data obtained by the AMR MHD simulation: one for a simulation on the coarse meshes alone and another with the refined meshes which provides even smaller-scale structures of magnetic fields (see Fig.2). The MHD simulation results are restricted to 2.5D, i.e. two dimensional geometry but three dimensional plasma velocities and magnetic fields. This assumption is reasonable since observations have shown that the extended solar flare arcades typically having much larger extend along the polarity-inversion line (PIL) than across the PIL.

The coordinate system is shown in Fig.1: the x and y-axis are directed along and perpendicular to the current sheet, respectively. The current sheet center is located at $y = 0$, while the z-axis is pointing along the PIL located at $(x = 0, y = 0)$. In this direction, every value is invariant i.e. $\partial/\partial z = 0$. The coarse resolution contains 6400×800 points in the vertical (x-axis) and right half of horizontal (positive y-axis) direction. A mirroring boundary is used at $y = 0$ for the left half box: ρ , u_x , u_z , B_y , B_z and U are symmetric while u_y , B_x are anti-symmetric. For the upper and right sides, free boundary conditions are used: all quantities should satisfy the von Neumann prescription $\partial/\partial \mathbf{n} = 0$ except of the normal magnetic field B_n and the total energy density U . B_n

and U are used to fulfill $\nabla \cdot \mathbf{B} = 0$. At the bottom, a symmetric boundary condition ($Q(-y) = Q(y)$) is used for ρ , B_x , B_z , U and the anti-symmetric relation $Q(-y) = -Q(y)$ is assumed for B_y . The plasma is always static $\mathbf{u} = 0$ at the bottom.

A generalized Harris-type current sheet is chosen as the initial state of the AMR MHD simulation (Bárta et al. 2010, 2011):

$$\begin{aligned} \mathbf{A}(x, y, z; t = 0) &= -B_{x0} \ln \left[\exp \left(\frac{y}{\omega_{cs}(x)} \right) + \exp \left(-\frac{y}{\omega_{cs}(x)} \right) \right] \hat{z} \\ B_z(x, y, z; t = 0) &= B_{z0} \\ \rho(x, y, z; t = 0) &= \rho_0 \exp \left(-\frac{x}{L_G} \right) \end{aligned} \quad (1)$$

where $\omega_{cs}(x)$ (Eq.(2)) shows the characteristic width at different height of the initial current sheet and $L_G = 120 \text{ Mm}$ is the scale height for a fully ionized hydrogen plasma:

$$\omega_{cs}(x) = \frac{d \cdot x^2 + x + x_0}{x + x_0} \quad (2)$$

and B_{x0} , B_{z0} , ρ_0 , d , x_0 are normalized quantities: $B_{z0} = 0.2$, $\rho_0 = 1.0$, $B_0 = \sqrt{B_{x0}^2 + B_{z0}^2} = 1.0$, $d = 0.003$ and $x_0 = 20.0$.

The x and y components of the magnetic field (B_x , B_y) are obtained from the magnetic vector potential \mathbf{A} as $\mathbf{B} = \nabla \times \mathbf{A}$. Note that the magnetic field strength slightly decreases via $\omega_{cs}(x)$ with height 'x' corresponding to the magnetic field in the solar corona balancing the gravity force (Eq.(6)). The initial magnetic field state is displayed in the left panel of Fig.1.

Compressible, resistive MHD equations (Eqs.(3) to (6)) are solved to describe the evolution of the plasma and magnetic fields (e.g., Priest 1984):

$$\frac{\partial \rho}{\partial t} + \nabla \cdot (\rho \mathbf{u}) = 0 \quad (3)$$

$$\rho \frac{\partial \mathbf{u}}{\partial t} + \rho(\mathbf{u} \cdot \nabla) \mathbf{u} = -\nabla p + \mathbf{J} \times \mathbf{B} + \rho \mathbf{g} \quad (4)$$

$$\frac{\partial \mathbf{B}}{\partial t} = -\nabla \times \mathbf{E} = \nabla \times (\mathbf{u} \times \mathbf{B} - \eta \mathbf{J}) \quad (5)$$

$$\frac{\partial U}{\partial t} + \nabla \cdot \mathbf{S} = \rho \mathbf{u} \cdot \mathbf{g} \quad (6)$$

where ρ is the plasma density, \mathbf{u} plasma velocity, \mathbf{B} magnetic field strength, \mathbf{E} electric field strength, η resistivity, \mathbf{g} gravitational acceleration at the photospheric level and p plasma pressure. The

current density \mathbf{J} , total energy density U and energy flux \mathbf{S} are defined as:

$$\mathbf{J} = \frac{\nabla \times \mathbf{B}}{\mu_0} \quad (7)$$

$$U = \frac{p}{\gamma - 1} + \frac{1}{2}\rho u^2 + \frac{B^2}{2\mu_0} \quad (8)$$

$$\mathbf{S} = \left(U + p + \frac{B^2}{2\mu_0} \right) \mathbf{u} - \frac{\mathbf{u} \cdot \mathbf{B}}{\mu_0} \mathbf{B} + \frac{\eta}{\mu_0} \mathbf{J} \times \mathbf{B} \quad (9)$$

where $\gamma_0 = \frac{5}{3}$ is the adiabatic coefficient for adiabatic condition and μ_0 is the vacuum magnetic permeability. The anomalous resistivity η in the Ohm's law (Eq.(5)) and in the energy flux \mathbf{S} (Eq.(9)) is chosen ad hoc to describe the sub-grid-scale dissipation effects of microphysical (kinetic) processes. It is switched on depending on the strength of the local current-carrier drift velocity $v_{CCD} = |\mathbf{J}|/(\epsilon\rho)$ compared to the critical threshold velocity v_{cr} (e.g., Bárta et al. 2011):

$$\eta(\mathbf{r}, t) = \begin{cases} 0 & |v_{CCD}| \leq v_{cr} \\ C \frac{v_{CCD}(\mathbf{r}, t) - v_{cr}}{v_0} & |v_{CCD}| > v_{cr} \end{cases} \quad (10)$$

Büchner & Elkina 2005, 2006 and Karlický & Bárta 2008 have confirmed this behaviour by means of Vlasov and PIC-code numerical simulation and derived both critical velocity v_{cr} and the coefficient C in Eq.(10).

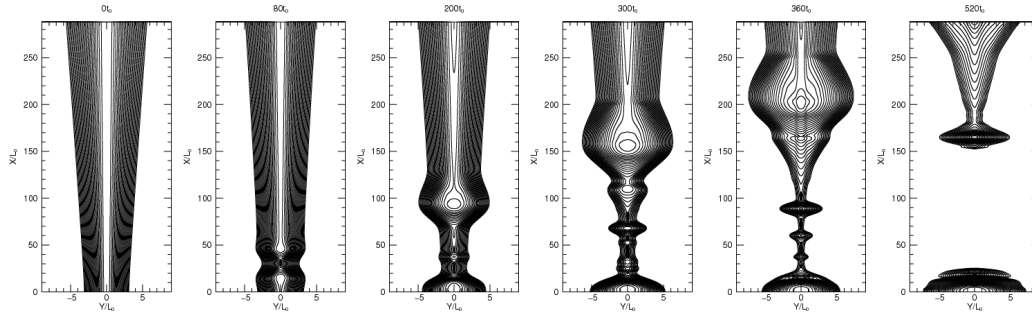


Fig. 1. Evolution of the in-plane magnetic field components of cascading magnetic reconnection in the CME-trailing current sheet obtained by high resolution 2.5D AMR MHD simulation. Panels from *left to right* show the initial state ($t = 0 t_0$), primary plasmoids ($t = 80 t_0$), secondary plasmoids ($t = 200 t_0$), third stage of plasmoids ($t = 300 t_0$), large scale magnetic islands mature state ($t = 360 t_0$) and last state ($t = 520 t_0$) where the erupted and disconnected magnetic field lines imply the appearance of a CME.

The AMR MHD simulation (Eqs.(3) to (6)) is carried out with normalized parameters: the normalizing length scale (half width of the current sheet at $x = 0$) is chosen to be $L_0 = 6.0 \times 10^5 m$, the normalizing magnetic field is $B_0 = 4.0 \times 10^{-2} T$ and the normalizing number density is $n_0 = 1.25 \times 10^{16} m^{-3}$ as well as $q_0 = |e|$ is taken as the normalizing charge. Other scaling parameters can be derived as: $V_0 = B_0 / \sqrt{\mu_0 n_0 m_0} = 7.80 \times 10^6 m/s$ (where $m_0 = m_p$ - proton mass and V_0 is the asymptotic value of the Alfvén velocity at $y \rightarrow \infty$, $x = 0$ and $t = 0$), The time is normalized by the Alfvén transit time $t_0 = L_0 / V_0 = 7.69 \times 10^{-2} s$. Furthermore there are $E_0 = V_0 B_0 = 3.12 \times 10^5 V/m$ and $\eta_0 = \mu_0 L_0 V_0 = 5.88 \times 10^6 \Omega \cdot m$. The asymptotic plasma beta parameter is $\beta = 0.1$ at ($y \rightarrow \infty$, $x = 0$). In the coarse resolution, the mesh sizes are $\Delta x = \Delta y = 0.045 L_0$. Hence the whole simulation domain extends over $(0, 288) \times (-36, 36) L_0^2$ in the x-y plane.

Fig.1 depicts the evolution of the in-plane magnetic fields. Total simulation is performed over $520 t_0$ when a CME is ejected through the upper boundary of the box (last panel of Fig.1). We pick out an already fragmented current sheet at $t = 360 t_0$ as the background electromagnetic fields since at this time step not only there are the most information of the refined smaller-scale magnetic structures but also after that no more additional magnetic islands are generated. No anomalous resistivity is switched on before $t = 420 t_0$.

In order to relate the electron acceleration to the resolution of the magnetic structures, we compare the acceleration in the coarsely and finely resolved magnetic fields. Fig.2 compares the magnetic structures obtained by the coarse (upper panels) and higher (lower panels) resolutions at $t = 360 t_0$. From left to right, increasing zoom-levels show the details of the magnetic structures. The right bottom panel depict the detail of smaller-scale magnetic structures obtained by the higher resolution.

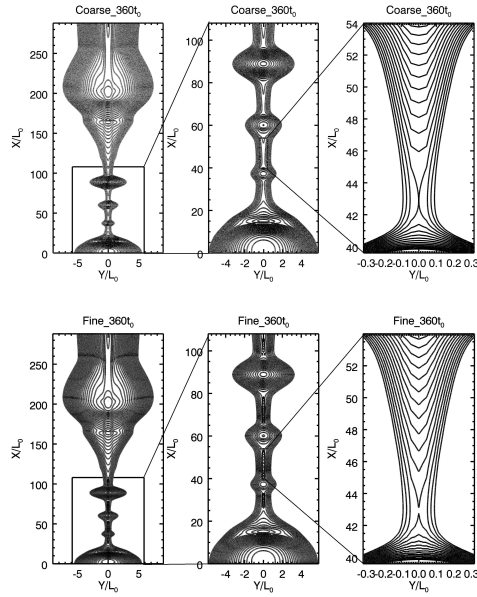


Fig. 2. Magnetic field lines at time $t = 360 t_0$. *Top line:* coarsely resolved magnetic structures. *Bottom line:* higher resolution simulation. *Left to right:* increasing zooms.

3. Methods Used

3.1. Test Particle Calculations

If the gyroradius ($r_{gy} = \frac{mv}{qB}$) and gyroperiod ($\propto 1/\omega_{gy} = \frac{2\pi m}{qB}$) of the particle are much smaller than the length scale of transverse gradients (r_{\perp}) and characteristic oscillation periods ($\propto 1/\omega_{os}$) of the ambient electromagnetic fields (i.e., $r_{gy}/r_{\perp} \ll 1$ and $\omega_{gy}/\omega_{os} \gg 1$), a guiding center approximation is valid. The motion of a magnetized charged particle can be decomposed into a drift of its guiding center and a gyration around this center (Northrop 1963).

The minimum magnetic field strength obtained by the AMR MHD simulations is $0.19 B_0$, for $10 MeV$ energized electrons, the corresponding gyroradius is $4.4 m$ only. The grid size even of the refined mesh ($\Delta x = \Delta y = 0.0045 L_0 = 2.7 km$) is much larger. As well as, in normalized Eqs.(11)

to (15) with the normalization values shown in Sect.2, a coefficient $\frac{m_0 V_0}{q_0 B_0 L_0}$ and its reciprocal arise in Eqs.(12) and (13). $\frac{m_0 V_0}{q_0 B_0 L_0}$ corresponds to the ratio of the particle gyroradius $\frac{m_0 V_0}{q_0 B_0}$ over the characteristic length L_0 or the particle gyro-period $\frac{m_0}{q_0 B_0}$ to the scaling time $t_0 = L_0/V_0$. If only $\frac{m_0 V_0}{q_0 B_0 L_0}$ is much smaller than unity, the guiding center approximation can be applied. In our study, it is only of the order of 10^{-6} . Hence, here we use the guiding center approximation to trace each electron.

Although only 0.01% and 0.45% electrons can be accelerated up to energies > 100 keV, for a high precision, a relativistic guiding center approximation is used:

$$\frac{d\mathbf{R}}{dt} = \mathbf{v}_D + \frac{(\gamma v_{\parallel})}{\gamma} \mathbf{b} \quad (11)$$

$$\begin{aligned} \mathbf{v}_D = & \mathbf{v}_E + \frac{m}{q} \frac{(\gamma v_{\parallel})^2}{\gamma k^2 B} [\mathbf{b} \times (\mathbf{b} \cdot \nabla) \mathbf{b}] + \frac{m}{q} \frac{\mu}{\gamma k^2 B} [\mathbf{b} \times (\nabla(kB))] \\ & + \frac{m}{q} \frac{(\gamma v_{\parallel})}{\gamma k^2 B} [\mathbf{b} \times (\mathbf{b} \cdot \nabla) \mathbf{v}_E] + \frac{m}{q} \frac{(\gamma v_{\parallel})}{\gamma k^2 B} [\mathbf{b} \times (\mathbf{v}_E \cdot \nabla) \mathbf{b}] \\ & + \frac{m}{q} \frac{\gamma}{\gamma k^2 B} [\mathbf{b} \times (\mathbf{v}_E \cdot \nabla) \mathbf{v}_E] + \frac{1}{\gamma c^2} \frac{E_{\parallel}}{\gamma k^2 B} (\gamma v_{\parallel}) [\mathbf{b} \times \mathbf{v}_E] \end{aligned} \quad (12)$$

$$\begin{aligned} \frac{d(\gamma v_{\parallel})}{dt} = & \frac{q}{m} \mathbf{E} \cdot \mathbf{b} - \frac{\mu}{\gamma} [\mathbf{b} \cdot \nabla(kB)] \\ & + (\gamma v_{\parallel}) \mathbf{v}_E \cdot [(\mathbf{b} \cdot \nabla) \mathbf{b}] + \gamma \mathbf{v}_E \cdot [(\mathbf{v}_E \cdot \nabla) \mathbf{b}] \end{aligned} \quad (13)$$

$$\gamma = \sqrt{\frac{c^2 + (\gamma v_{\parallel})^2 + 2\mu B}{c^2 - v_D^2}} \quad (14)$$

$$\frac{d\mu}{dt} = 0 \quad (15)$$

here \mathbf{R} , \mathbf{v}_D , v_{\parallel} , γ and \mathbf{b} are the guiding center position vector, the perpendicular drift velocity, the velocity along the magnetic field, the relativistic factor ($\frac{c}{\sqrt{c^2 - v^2}}$) and the magnetic field direction unity vector $\mathbf{b} = \frac{\mathbf{B}}{B}$, respectively. In the expression for the drift velocity \mathbf{v}_D in Eq.(12), the term \mathbf{v}_E corresponds to the local $\mathbf{E} \times \mathbf{B}$ drift velocity $\mathbf{v}_E = \frac{\mathbf{E} \times \mathbf{B}}{B^2}$. Other terms are the magnetic curvature drift velocity and the magnetic gradient drift velocity as well as higher order drifts. The factor $k = \sqrt{1 - \frac{v_E^2}{c^2}}$ relates the electromagnetic field values to the reference frame moving with the velocity \mathbf{v}_E . Finally, $\mu = \frac{(\gamma v_{\perp})^2}{2B}$ is the relativistic magnetic moment per mass unit where v_{\perp} is the particle gyration velocity perpendicular to \mathbf{B} . The electron energy is expressed using the relativistic γ -factor as $E = (\gamma - 1)mc^2$. The set of Eqs.(11) to (15) are solved utilizing a fourth-order Runge-Kutta scheme. The field values between the grid points are interpolated along the electron trajectories with 2D linear interpolation.

4.752×10^5 test electrons are initially uniformly distributed along the current sheet ($0 < x < 108 L_0, y = 0$) at 2400 points with 22 different initial velocities from 0.0 to $21.0 v_{th}$ and 9 different initial pitch angles from 0 to π . Here v_{th} is the electron thermal velocity for a typical coronal temperature of 10^6 K: $0.76V_0 \cong 6 \times 10^3$ km/s. Every electron is traced for up to $10t_0$ (~ 0.769 s) or until it

leaves the simulation domain, whatever happens first. Not that this time is shorter than the time scale of essential magnetic field changes in the MHD simulations.

3.2. Spectrum Distribution function of accelerated electrons

To obtain the energetic electron distribution function, we use the fact that the solar corona is practically collisionless. Hence according to Liouville's theorem, the particle distribution function keeps constant along the particle trajectory: $f(E, A, \mathbf{r}, t) = f(E_0, A_0, \mathbf{r}_0, t_0)$. This allows to calculate the electron distribution function $f(E, A, \mathbf{r}, t)$ at the place where HXR are expected to be generated by Bremsstrahlung of energetic electrons.

3.3. HXR Emission

Knowing the local plasma number density and electron distribution function, the hard X-ray emissivity $I(\epsilon)$ integrated over all contributing electrons can be calculated in the frame work of the thin target model (Brown 1971) as:

$$I(\epsilon) = \sum_{E > \epsilon}^{\infty} n(\mathbf{r}) v(\mathbf{r}) \sigma_B(\epsilon, E) f(E, A, \mathbf{r}, t) \quad (16)$$

Here E , A , \mathbf{r} and $v(\mathbf{r})$ are the energy, pitch angle, position and velocity of the electron at the time t , $n(\mathbf{r})$ is the local plasma number density, ϵ is the radiated photon energy, $f(E, A, \mathbf{r}, t)$ is the electron distribution function at the position of interest place and time, while σ_B is the cross section of the Bremsstrahlung process. For a simple approximation, we take the Bethe-Heitler formula for the Bremsstrahlung cross section (Bethe & Heitler 1934; Brown 1971):

$$\sigma_B(\epsilon, E) \propto \frac{1}{\epsilon E} \ln \left[\frac{1 + \sqrt{1 - \frac{\epsilon}{E}}}{1 - \sqrt{1 - \frac{\epsilon}{E}}} \right] \quad (17)$$

Note that the Bethe-Heitler formula applies only to particle energies less than 100 keV. In this investigation, for both kinds of magnetic fields resolution, more than 99% of the electrons are accelerated to energies less than 100 keV, i.e. the Bethe-Heitler formula still can give a high accuracy here.

4. Results

Depending on the locations of the simulated electrons at 10 t_0 , three groups of electrons can be identified: those trapped in the magnetic islands; those precipitating to the chromosphere and the ones being ejected into the interplanetary space. There is no electron escaping from the left and right sides of the simulation domain. We concentrate our analysis on the trapped (Sect.4.1) and precipitating (Sect.4.2) electrons.

4.1. Trapped Electrons

More than 80% of simulated electrons are still trapped in the magnetic islands along the current sheet by $10 t_0$. This highly dynamical and complex magnetic field structure provides a very effective trapping mechanism of energetic electrons for the coronal HXR sources.

4.1.1. Acceleration dependence on initial conditions and magnetic field resolution

The acceleration of electrons in the convective (or induced) electric field $\mathbf{E} = -\mathbf{u} \times \mathbf{B}$ is sensitive to the initial position, velocity, and pitch angle of injected electrons and the fine structure of the magnetic field. The upper panels of Fig.3 depict the dependence of the energy gain on the initial conditions and the magnetic field resolution. The lower panels show the corresponding projected results.

In general, the electron acceleration is more efficient in magnetic fields with better resolved small scale structures for the larger magnetic curvatures and gradients accessible. The maximum final kinetic energy of trapped electrons is at most of the order of 100 keV in coarsely resolved magnetic fields, but it can be up to 470 keV if smaller-scale magnetic structures are taken into account, corresponding to a maximum energy gain of 53 keV and 420 keV for the coarsely and finely resolved fields respectively.

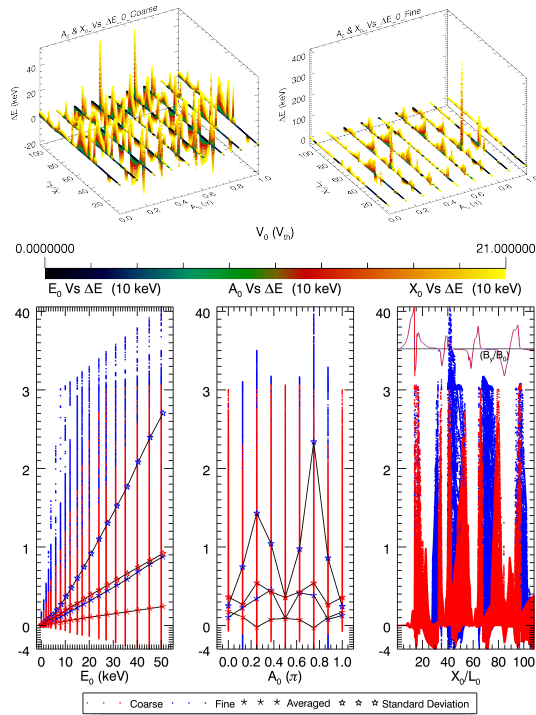


Fig. 3. Dependence of the electron kinetic energy gain (ΔE) on the initial pitch angle (A_0), velocity (v_0) and position (x_0) for two differently resolved magnetic field structures. Each point represents one electron. The *upper* panels show the 3D result with the initial velocity color coded. The *lower* panels show the corresponding projected results and the averaged value (\star lines) and standard deviation of the energy gain (\star lines) in the initial energy and pitch angle spaces. B_y along the current sheet center is depicted in the bottom-right panel. The *red* and *blue* colors are used to distinguish the results in the coarsely and finely resolved magnetic fields, respectively. Note that there are three different scales in the y-axis for $\Delta E < 0$, $0 < \Delta E < 3 \text{ keV}$ and $\Delta E > 3 \text{ keV}$.

From left to right the bottom panels of Fig.3 depict the dependence of acceleration efficiency on the electron initial energy, pitch angle and position, respectively. The kinetic energy gain increases with the increase of the initial energy, which is consistent with the results of Guo et al. 2010. It is interesting to note that both the mean and the standard deviation of the energy gain are roughly proportional to the initial energy and the acceleration efficiency of the finely resolved case is about 3 times higher than the coarse one. The dependence of the electron energy change on the initial pitch angle and position, however, is more or less chaotic due to the complex field structures. Different from Karlický & Kosugi 2004 where the betatron process dominates, here the most energetic electron is not associated with an initial pitch angle of 90° any more. The acceleration symmetry with respect to the 90° pitch angle is also broken when the magnetic fields are better resolved. The lower-right panel of Fig.3 also shows the magnetic field component B_y along the current sheet center $y = 0$, which can be used to identify the magnetic X- and O-points with $B_y = 0$. The most efficient acceleration appears to be associated with electrons injected close to the X-points that contain larger magnetic gradients and smaller magnetic curvature radii.

4.1.2. Energy gain

The guiding center approach decomposes particle energy into components parallel and perpendicular to the magnetic field and the part associated with the guiding center drift in the direction perpendicular to the magnetic field. The maximum drift velocity v_D (Eq.(12)) is $1.40 v_{th}$ and $0.97 v_{th}$ in the coarsely and finely resolved magnetic fields, which is negligible comparing with the other two components.

Considering that the anomalous resistivity is not switch on ($\mathbf{E} \cdot \mathbf{b} = 0$) and $\mathbf{v}_D \cong \mathbf{v}_E$, $k \cong 1$, Eqs.(13), (15) and $\mu = \frac{(\gamma v_\perp)^2}{2B}$ give:

$$\frac{1}{2} \frac{d(\gamma v_\parallel)^2}{dt} = -\mu v_\parallel [\mathbf{b} \cdot \nabla B] + (\gamma v_\parallel)^2 \mathbf{v}_E \cdot [(\mathbf{b} \cdot \nabla) \mathbf{b}] \quad (18)$$

$$\begin{aligned} \frac{1}{2} \frac{d(\gamma v_\perp)^2}{dt} &= \frac{d\mu B}{dt} = \mu \frac{dB}{dt} \\ &= \mu v_\parallel [\mathbf{b} \cdot \nabla B] + \mu \mathbf{v}_E \cdot \nabla B \end{aligned} \quad (19)$$

So the energy evolution of an electron in the guiding-center limit is given by:

$$\begin{aligned} \frac{dE_k}{dt} &\propto \frac{d(\gamma v_\parallel)^2 + (\gamma v_\perp)^2}{dt} \\ &= \mu \mathbf{v}_E \cdot \nabla B + (\gamma v_\parallel)^2 \mathbf{v}_E \cdot [(\mathbf{b} \cdot \nabla) \mathbf{b}] \end{aligned} \quad (20)$$

Fig.4 exhibits the spacial distributions of the acceleration rates in Eqs.(18) and (19): $(\mathbf{b} \cdot \nabla B)/(2B)$ (the middle panel), $(\mathbf{v}_E \cdot \nabla B)/(2B)$ (the left panel) and $\mathbf{v}_E \cdot [(\mathbf{b} \cdot \nabla) \mathbf{b}]$ (the right panel) in the coarse calculation domain (corresponding to the top-middle panel of Fig.2), note that these distributions are quite similar between the coarsely and finely resolved magnetic fields.

Eqs.(18) and (19) depict the parallel magnetic gradient ($\mathbf{b} \cdot \nabla B$) can change both the parallel and perpendicular energies of electrons, but they cancel out each other in the total energy evolution (20). The overall energy change is dominated by the perpendicular magnetic gradient ($\mu \mathbf{v}_E \cdot \nabla B$) and curvature ($(\gamma v_{\parallel})^2 \mathbf{v}_E \cdot [(\mathbf{b} \cdot \nabla) \mathbf{b}]$), which are proportional to the electron energy due to μ and $(v_{\parallel})^2$, respectively. The increase of the electron acceleration with the increasing initial energy is therefore expected (see the lower-left panel of Fig.3). (In addition, trapped electrons with larger initial velocities bounce and pass accelerators more frequently to gain more energies.)

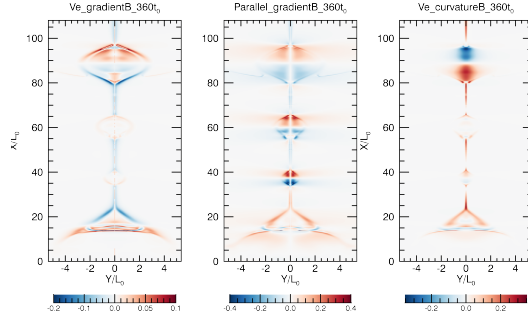


Fig. 4. Spatial distributions of perpendicular (*left panel*), parallel (*middle panel*) gradient and perpendicular curvature (*right panel*) in Eqs.(18) and (19) of the coarsely resolved magnetic fields.

Also due to the combined actions between the magnetic gradient and curvature in Eq.(20), the favourable initial pitch angles (shown in the lower-middle panel of Fig.3) are not 0, 180° or 90° which correspond to acceleration dominated only by magnetic curvatures ($(\gamma v_{\parallel})^2 \mathbf{v}_E \cdot [(\mathbf{b} \cdot \nabla) \mathbf{b}]$) or gradients ($\mu \mathbf{v}_E \cdot \nabla B$), respectively. No favourable initial pitch angle with 0, 180° or 90° indicates that the perpendicular magnetic gradient and curvature acceleration efficiencies are comparable with each other in this complex magnetic field structure no matter what resolution of magnetic fields are used. These favourable initial pitch angles also change with the magnetic field resolution. The acceleration asymmetry around initial pitch 90° (the bottom-middle panel of Fig.3) is due to the non-symmetric acceleration factors around the current sheet center in ($\mu \mathbf{v}_E \cdot \nabla B$) and $(\gamma v_{\parallel})^2 \mathbf{v}_E \cdot [(\mathbf{b} \cdot \nabla) \mathbf{b}]$ by the third dimension of electromagnetic fields in 2.5D symmetric current sheet geometry. The acceleration symmetry is weakly broken for the coarsely resolved case.

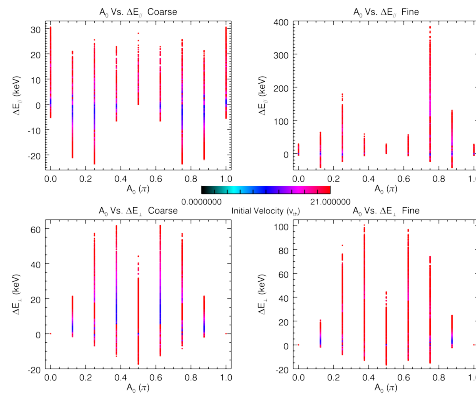


Fig. 5. Parallel (ΔE_{\parallel} in *top line*) and perpendicular (ΔE_{\perp} in *bottom*) acceleration symmetry about the initial pitch angle 90°. *Left panels*: case of the coarsely resolved magnetic fields. *Right panels*: highly resolved ones. Every trapped electron (shown by one '*' point) is color-coded by its initial velocity. The corresponding color-code is shown in the middle.

Fig.5 shows electron acceleration symmetry around the initial pitch angle 90° for the parallel and perpendicular energy gain components. With the details of the parallel and perpendicular acceleration, one can see that electron parallel and perpendicular acceleration are not exactly symmetric around the initial pitch angle 90° in both the coarsely and finely resolved magnetic fields. The symmetry is better preserved in the coarsely resolved fields due to the smoothing effects (see the bottom-middle panel of Fig.3).

The term $\mu v_{\parallel}(\mathbf{b} \cdot \nabla B)$ in Eqs.(18) and (19), however, is not influenced by the third dimension of electromagnetic fields, hence it is symmetric around the current sheet center at the beginning. In other words, the non-symmetric acceleration in the parallel and perpendicular direction (see the top and bottom panels of Fig.5, respectively) are due to non-symmetric $(\mu \mathbf{v}_E \cdot \nabla B)$ and $(\gamma v_{\parallel})^2 \mathbf{v}_E \cdot [(\mathbf{b} \cdot \nabla) \mathbf{b}]$ around the current sheet center, respectively. For the coarsely resolved case, the acceleration is dominated by the perpendicular component, the reverse is true for the finely resolved case. Meanwhile non-symmetric parallel acceleration (i.e. non-symmetric $|v_{\parallel}|$) can enhance the asymmetry in both the parallel and perpendicular acceleration (see Eqs.(18) and (19)).

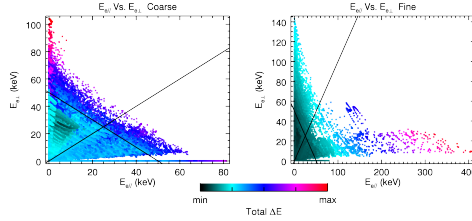


Fig. 6. Comparison between the final parallel (E_{\parallel}) and perpendicular (E_{\perp}) kinetic energy of trapped electrons in the coarsely (*left panel*) and finely (*right panel*) resolved magnetic fields. Each electron is color-coded by its total kinetic energy change (ΔE). The *black lines* in each panel correspond to ' $E_{\perp} = E_{\parallel}$ ' and ' $E = E_{\perp} + E_{\parallel} = 50$ keV'.

Fig.6 shows the distribution of the trapped electron acceleration in the $(E_{\parallel}, E_{\perp})$ plane. The distribution of the strongly accelerated electrons is highly anisotropic. It is dominated by the perpendicular and parallel kinetic energy components for the coarsely and finely resolved magnetic fields, respectively. While for the weakly accelerated electrons, they still roughly keep their initial isotropic distribution. For electrons initially moving only along magnetic field lines (with an initial pitch angle 0 or 180°), they do not have acceleration in the perpendicular direction. In this condition, however, the parallel acceleration is a little stronger in the coarsely resolved magnetic fields (maximum finale energy 81 keV) than that in the fine case with maximum finale energy 79 keV.

4.1.3. Characteristic trajectories

To better understand the details of the electron acceleration processes, the first row of Fig.7 and second row of Fig.8 depict the trajectory and energy evolution of the most energetic electrons in the coarsely ($v_0 = 21 v_{th}$, $A_0 = 5/8\pi$, $x_0 = 97.56 L_0$) and finely ($v_0 = 21 v_{th}$, $A_0 = 3/4\pi$, $x_0 = 41.58 L_0$) resolved magnetic fields, respectively, and all panels in Fig.8 have the same initial conditions as the corresponding panels in Fig.7.

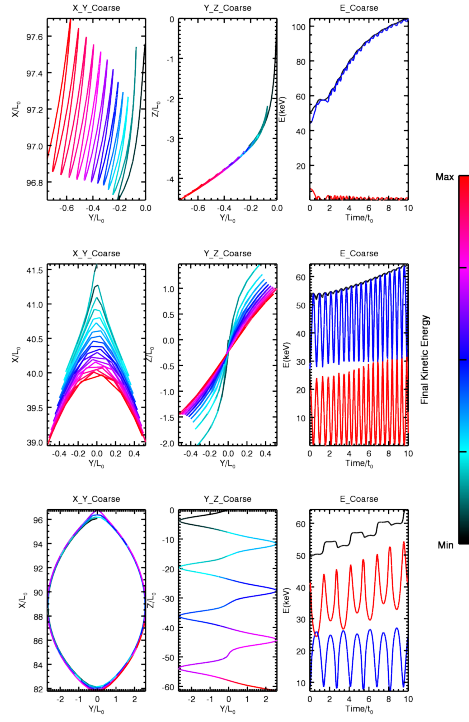


Fig. 7. Trajectory and energy evolution for three characteristic trapped electrons in the coarsely resolved magnetic fields. Panels in the *first* and *second* column show the electron trajectory in the xy and yz plane, they are color-coded by the total kinetic energy profile. Panels in the *third* column show the electron total kinetic (black line), parallel (red line) and perpendicular (blue line) energy evolution.

For the coarsely resolved case, the most efficient acceleration is dominated by the increase of the perpendicular energy component for the positive perpendicular magnetic gradient $\mu \mathbf{v}_E \cdot \nabla B$ above $95 L_0$ (see the left panel of Fig.4). Also the slightly decreasing parallel energy is due to the negative perpendicular curvature $\mathbf{v}_E \cdot [(\mathbf{b} \cdot \nabla) \mathbf{b}]$ there (see the right panel of Fig.4). With the same initial conditions, the corresponding electron in the finely resolved magnetic fields gain more energy (see the first row in Fig.8).

For the finely resolved case, the most efficient acceleration happens to the parallel energy component with slightly increased perpendicular energy when the electron are trapped in the magnetic island (around $x = 37 L_0$) and accelerated again and again with its circulating motions by the positive perpendicular magnetic curvature $\mathbf{v}_E \cdot [(\mathbf{b} \cdot \nabla) \mathbf{b}]$ (located at the thin layer in the central current sheet above $x = 40 L_0$, corresponding to the step-like increased displacement in the z direction, see the final kinetic energy color-coding yz -trajectory projection in the second row of Fig.8) and gradient $\mu \mathbf{v}_E \cdot \nabla B$ (located around $x = 40 L_0$). As expected, in the coarsely refined magnetic fields without the smaller-scale magnetic field structures, trajectory and acceleration of the corresponding electron are totally changed. This electron is mirror-trapped and cannot circulate in the magnetic island and move systematically in the z direction.

In the right panel of Fig.4, one can see the largest perpendicular curvature acceleration region is located at around $x = 85 L_0$, however, the strongest energetic electron is not launched there. That is due to the cancellation between the perpendicular curvature acceleration and deceleration when electron circulates in the magnetic island at $x \sim 90 L_0$. Electrons in the third row of Fig.7 and Fig.8

are chosen to reveal the acceleration characteristics around $x = 90 L_0$. These two electrons also have the same initial conditions: $v_0 = 21 v_{th}$, $A_0 = 7/8\pi$ and $x_0 = 96.075 L_0$. Their color-coded yz -trajectory projection in the third row of Fig.7 and Fig.8 prove the above discussion and their energy gains are mainly due to the parallel acceleration by the perpendicular magnetic curvature. Furthermore these two electrons have the same trajectory and energy evolution, i.e., there is no influence coming from the magnetic field resolution, since no refined smaller-scale magnetic structures are found along their trajectories between $x = 81 - 97 L_0$.

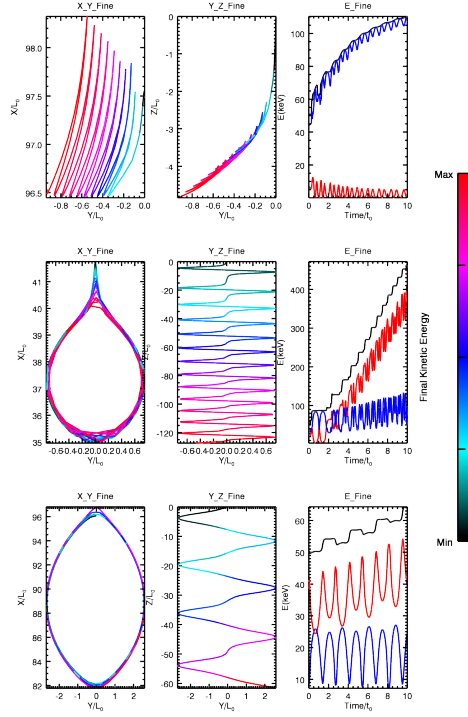


Fig. 8. Trajectory and energy evolution of electrons launched with the same initial conditions as the corresponding one in Fig.7 but in finely resolved magnetic fields.

Energy oscillation between parallel and perpendicular energies in each characteristic electron energy evolution profile (the last column of Fig.7 and Fig.8) is due to the parallel magnetic gradient $v_{||}(\mathbf{b} \cdot \nabla B)$ in Eqs.(18) and (19) when electron passes the positive and negative parallel magnetic gradient regions in turn or electron is mirrored with alternate parallel velocity in the parallel and anti-parallel direction. Each condition can be found in Fig.7 and Fig.8. While the magnitude of this oscillations is due to magnitude of the parallel magnetic gradients $\mathbf{b} \cdot \nabla B$ along electron trajectory (see the middle panel of Fig.4).

4.1.4. Comparison with Observations

More than 60% of trapped electrons are accelerated ($\Delta E > 0$) and more than 50% of them have kinetic energies larger than 10 keV. These energetic electrons can produce HXR by Bremsstrahlung (note that the HXR range is 10 – 400 keV). In the framework of the thin target model (Brown 1971) and using the Bethe-Heitler formula for the Bremsstrahlung cross section (Bethe & Heitler

1934; Brown 1971, see details in Sec.3.3), we derive the HXR spectrum of these energetic trapped electrons in order to compare our results with solar flare HXR observations.

Since the initial electron distribution function in the solar atmosphere is not known, we consider three different initial distribution functions as:

$$f(E_0, A_0, \mathbf{r}_0, t_0) \propto \begin{cases} E_0^0 \text{ (or Constant)} \\ E_0^{-3} \\ \text{Maxwell-Boltzmann} \end{cases} \quad (21)$$

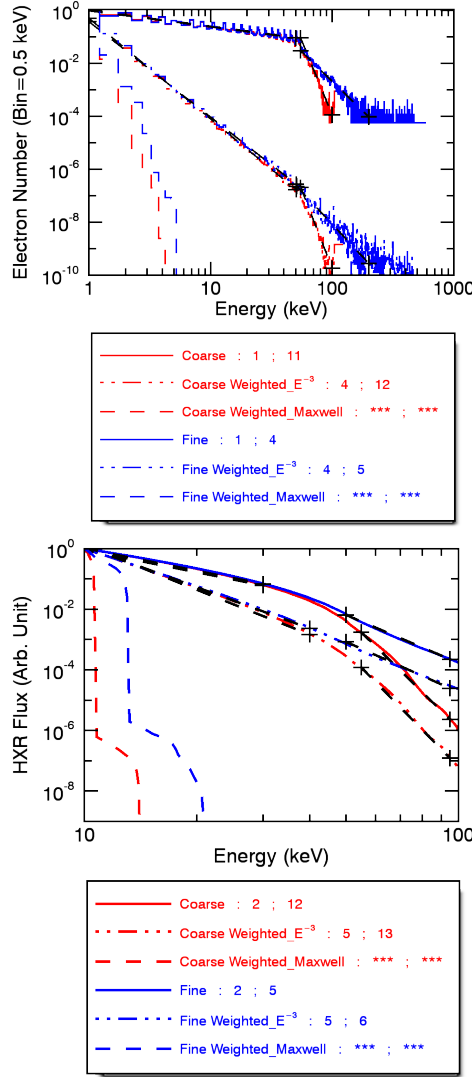


Fig. 9. Electron (*top*) and HXR (*bottom*) spectra of energetic trapped electrons in the coarsely (*red* lines) and finely (*blue* lines) resolved magnetic fields with three different initial distribution functions - constant (*solid* lines), power-law -3 (*dash-dot* lines) and Maxwellian at 10^6 K (*dashed* lines). The spectral indices are for the ranges marked with the black dashed lines embraced by two plus signs at two ends and their values are shown under each panel: the first one for electron and photon energies below 50 keV and the second one for the energies between 50 keV and 100 keV.

The resulting electron and HXR spectra and spectral indices (below and above 50 keV) after acceleration ($t = 10 t_0$) are depicted in the top and bottom two panels of Fig.9, respectively. In approximation, the relationship between the electron (γ_e) and corresponding HXR (γ_{HXR}) spectral

indices agree well with the relationship $\gamma_{HXR} = \gamma_e + 1$ in the thin target model. The influence from the ambient plasma number density n_r (Eq.(16)) is very small due to its small normalized range [0.3 – 1.8] in both differently resolved magnetic fields, while the HXR flux at 100 keV differs by more than 4 orders of magnitude for these two cases (see the bottom panel of Fig.9). Note that the HXR spectral indices, calculated from an initial Maxwell-Boltzmann distribution function for $T = 10^6$ K, are too large to match any observed HXR spectrum. For the cases with a power-law distribution initially (e.g., Karlický & Bárta 2006), one may treat the electron acceleration as a diffusion in 2D energy space. Since the diffusion coefficient is approximately proportional to the energy, this explains the difference by one of the spectral indexes of the injected and accelerated electrons below the maximum injection energy of ~ 50 keV. Above 50 keV, the acceleration in the finely resolved magnetic field is much more efficient than that in the coarsely resolved magnetic field, we have a harder spectrum (~ 6) for the finely resolved case. The corresponding HXR spectral indexes are consistent with the observed values for small flares (whose HXR spectral indices can be as soft as ≥ 7 , see Aschwanden 2002).

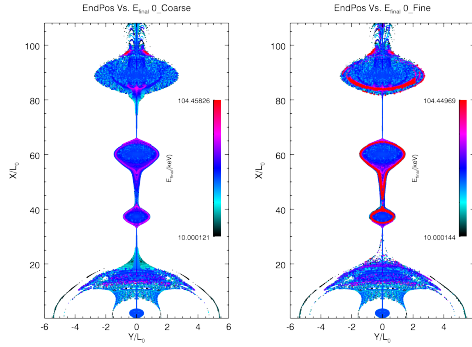


Fig. 10. Final locations of trapped electrons with final kinetic energies > 10 keV at $t = 10t_0$. They are color-coded by their final kinetic energies. *Left* and *right* panels correspond to the coarsely and finely resolved magnetic fields. Note that the electrons with final kinetic energy > 105 keV are shown only by red asterisk points in the better resolved magnetic fields.

Besides the HXR spectra, fine structures (bright spots) along the current sheets trailing CMEs or eruptive filaments were observed (e.g., by Ciaravella et al. 2002; Ko et al. 2003; Savage et al. 2010). These bright spots should come from energetic trapped electrons. Fig.10 shows the final locations of these trapped electrons with final kinetic energies > 10 keV which will brighten the magnetic island in the current sheet that may be associated with the observed hot spots. Furthermore depending on the evolution of these magnetic islands, the bright spot located at $x = 90 L_0$ moves upwards away from the sun while others fall back to the sun. This evolution agrees well with the observed upward (Ciaravella et al. 2002; Ko et al. 2003; Savage et al. 2010) and downward (Ko et al. 2003; Savage et al. 2010) moving bright spots in CME-trailing current sheets.

4.2. Precipitating Electrons

A second observable feature which can be derived from our calculations are the emission produced by the energetic precipitating electrons. They can precipitate to the solar chromosphere and be

related to the observed footpoint HXR signatures there. We first study the acceleration dependence of precipitating electrons on the initial conditions (velocity, pitch angle and position). The results are shown in Fig.11.

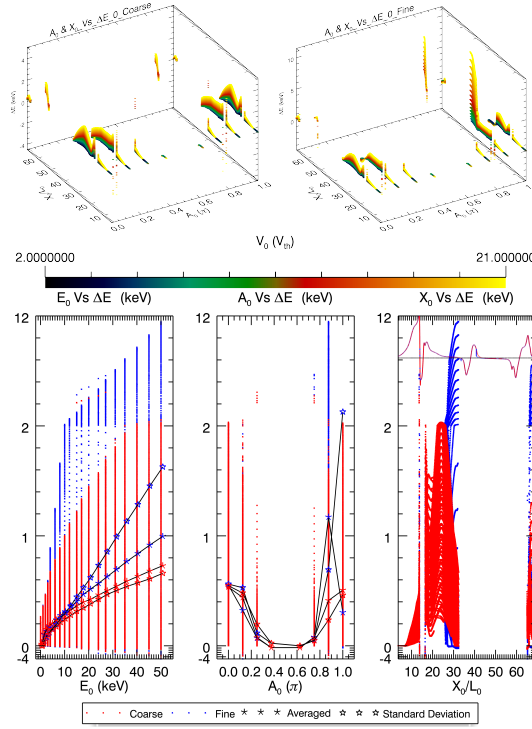


Fig. 11. Same as Fig.3 but for precipitating electrons. Here three different scales in the y-axis are also used for $\Delta E < 0$, $0 < \Delta E < 2$ keV and $\Delta E > 2$ keV.

4.2.1. Initial condition dependence

Similar to electrons trapped in the current sheet, acceleration of precipitating electrons also strongly depends on their initial (velocity, pitch angle and position) conditions. The acceleration efficiency increases with the increase of the energy and the overall acceleration is more efficient in finely resolved magnetic field. However the acceleration is much less efficient than those trapped electrons. The maximum energy gain is only a few keV and about 10 keV for the coarsely and finely resolved magnetic fields respectively. The dependence of the energy gain on the initial pitch angle and position show that only electrons in a few channels can escape from the acceleration site and injected into the chromosphere. As expected, electrons moving along magnetic field line are more likely to escape than those with a pitch angle close to 90° . However, only a small portion ($< 12\%$) of electrons can precipitate into the chromosphere.

The bottom right panel of Fig.11 depicts that a large portion of precipitating electrons start near to X-points. But no electron escapes from the X-points near $x = 42 L_0$ and $x = 97 L_0$. Since the magnetic islands below this two X-points is not symmetric about their center - O-points: their upper parts are smaller than the lower parts (see the whole B_y plots in the bottom right panel of Fig.3). Current sheet center launched electrons are easily reflected or trapped by this geography

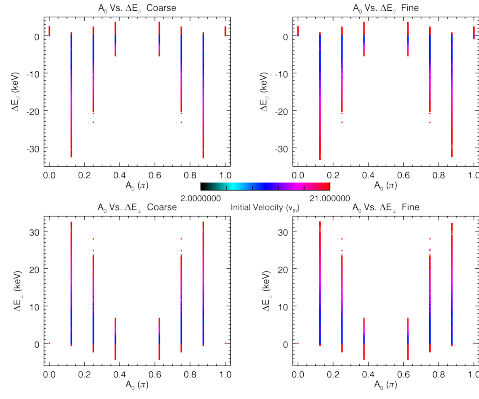


Fig. 12. Same as Fig.5 but for precipitating electrons.

(see the characteristic trajectories of trapped electrons launched near $x = 42 L_0$ in the middle-line of Figs.7 and 8).

4.2.2. Acceleration properties

Although there are the same reasons for the asymmetric acceleration around the initial pitch angle 90° in the finely resolved magnetic fields between trapped and precipitating electrons, acceleration asymmetry of precipitating electrons is much weaker than that of trapped electrons (comparing Fig.5 with Fig.12).

The total acceleration of precipitating electrons also is much weaker than that of trapped electrons, see the ' $E = 50 \text{ keV}$ ' parts of Fig.6 and Fig.13, especially the coarse case for precipitating electrons in Fig.13. The final kinetic energy E_e of the most energetic precipitating electrons is a little more than 50 and 60 keV in the coarsely and finely resolved magnetic fields, respectively, i.e., all precipitating electrons have final kinetic energies $E_e < 100 \text{ keV}$. Different from trapped electrons in Fig.6, here most precipitating electrons still keep their initial energies shown as stripes parallel to ' $E = 50 \text{ keV}$ '

Acceleration difference between trapped and precipitating electrons is mainly contributed by the acceleration in the parallel direction. Precipitating electrons have stronger deceleration than acceleration in the parallel direction (see the top panels of Fig.5 and Fig.12), i.e., the acceleration of precipitating electrons are mainly coming from the perpendicular direction independent on the magnetic field resolution (see also Fig.13). For a stronger parallel acceleration, electron should stay longer around the current sheet center where has larger magnetic curvatures than other places, while precipitating electrons are ejected out of the current sheet before they can reach higher energies.

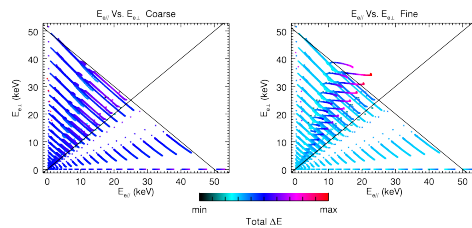


Fig. 13. Same as Fig.6, but for precipitating electrons.

On the whole the acceleration differences of precipitating electrons between in the coarsely and finely resolved magnetic fields are not so many as that of trapped electrons, since precipitating electrons spend most of their time far away from the central current sheet and the better resolved magnetic structures are located only near the current sheet center.

4.2.3. characteristic trajectory of precipitating electron

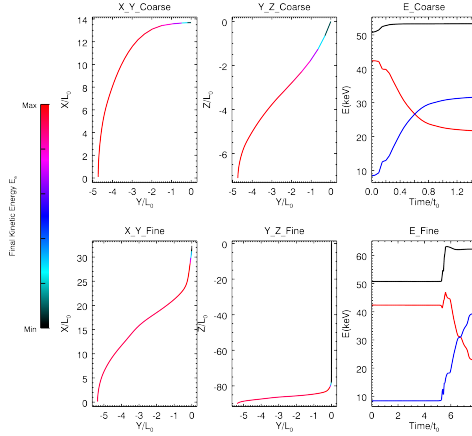


Fig. 14. Trajectory projection and energy evolution of the most energetic precipitating electron with initial velocity $v_0 = 21 v_{th}$ and pitch angle 157.5° in the coarsely (*left* panel) and finely (*right* panel) resolved magnetic fields. Trajectories are color-coded according to the local electron total kinetic energy.

Top and bottom lines of Fig.14 show the trajectory and energy evolution of the most energetic precipitating electron in the coarsely and finely resolved magnetic fields, respectively. Their xy and yz trajectory projections (along the magnetic field lines only) prove their strongly magnetized condition. Also the energy profiles in the last column of Fig.14 depict the different acceleration properties in the coarsely and finely resolved magnetic fields: their acceleration sites are still in the current sheet center by the perpendicular magnetic curvatures $\mathbf{v}_E \cdot [(\mathbf{b} \cdot \nabla)\mathbf{b}]$ and gradients $\mathbf{v}_E \cdot \nabla B$. After they leave there is no acceleration any more, there parallel magnetic gradient $v_{||}(\mathbf{b} \cdot \nabla B)$ is stronger than the other two terms (see Fig.4).

Also because of the single sign of the parallel magnetic gradients and direction of parallel velocity along precipitating electron trajectory, precipitating electrons do not have frequent energy oscillation as that of the characteristic trapped electrons in Fig.7 and Fig.8.

4.2.4. Comparison with UV and EUV observations

The low energies of the precipitating electrons in the convective electric fields can not cause HXR emissions but ribbons of UV and EUV brightening (Fletcher et al. 2011). Fig.15 depicts the spatial distribution of the electrons precipitating to the chromosphere at the end of calculation ($t=10 t_0$, top panels) and their evolution with time (panels in the last two lines). As the figure shows the ribbons exhibit a anti-symmetric geometry around the PIL.

This two ribbons are related to the initial pitch angles of precipitating electrons: electron with an initial pitch angles $> 90^\circ$ ($< 90^\circ$) precipitates into one (the other) branch. This kind of initial

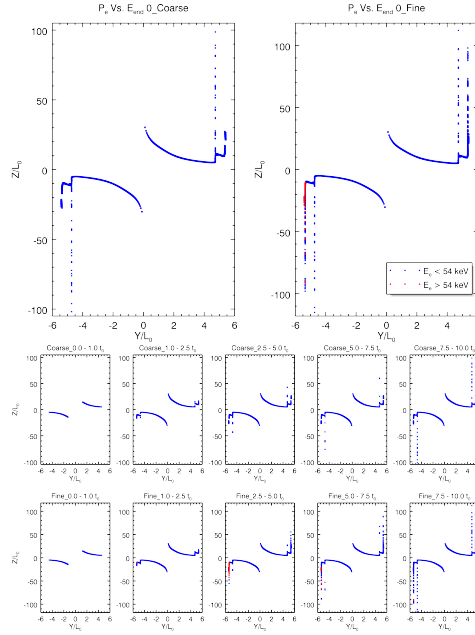


Fig. 15. Chromosphere locations of precipitating electrons at $t=10 t_0$ (top line) and their evolution (bottom two lines), color-coded by their final kinetic energies (E_e - Blue '*' for $E_e < 54 \text{ keV}$ and red '*' for $E_e > 54 \text{ keV}$) separately in the coarsely and finely resolved magnetic islands.

pitch angle dependence is attributed to the weak parallel accelerations by the perpendicular magnetic curvature $(\gamma v_{\parallel})^2 \mathbf{v}_E \cdot [(\mathbf{b} \cdot \nabla) \mathbf{b}]$ (Eq.(18)) which cannot accelerate electron into the direction anti-parallel to its initial velocity. Because of the non-symmetric acceleration around the initial pitch angle 90° of precipitating electrons in the finely resolved magnetic fields, more efficiently accelerated precipitating electrons are with initial pitch angles 0.875π ($> 90^\circ$). Hence more accelerated ($E_e > 54 \text{ keV}$) precipitating electrons are only located at one branch of the ribbon geometry with finely resolved smaller-scale magnetic structures (the top-right panel of Fig.15). Some of the observed asymmetry between two footpoints therefore may be attributed to the acceleration process. While the chromosphere energy distribution of precipitating energized electrons, accelerated by coarsely resolved magnetic structures, are more anti-symmetric with respect to the PIL (the top-left panel in Fig.15).

Also with the chromospheric location evolution of the precipitating electrons (panels in the last two lines of Fig.15), one can find their locations along the chromospheric ribbons depend on their initial positions also: electrons started closer to the sun surface precipitate closer to the PIL, earlier in the chromosphere and have shorter displacements along z-axis (or PIL). At the same initial position, electrons with larger initial energies correspond to larger final kinetic energies and parallel velocities which lead electron to reach chromosphere earlier (see Fig.16).

Fig.16 shows that fluxes of electrons with higher energies evolve faster and reach peaks earlier than those of lower energy electrons. The time scale of the flux peak of precipitating electrons with final kinetic energies $> 50 \text{ keV}$ indicates precipitating electrons are accelerated less than $1.0 t_0 < 0.1 \text{ s}$. The refined magnetic field structures are mainly located above $x = 25 L_0$, hence at the beginning (before $1.5 t_0$) there is no acceleration difference between the coarsely and finely resolved magnetic fields for precipitating electrons.

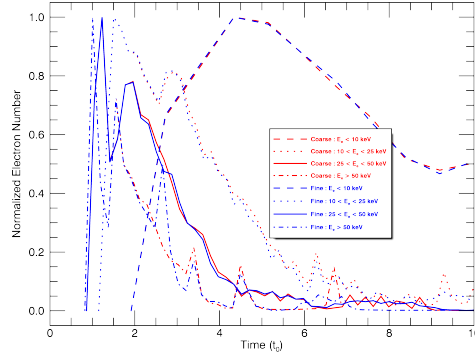


Fig. 16. Lightcurve of precipitating electrons for four energy ranges: $E_e < 10$ keV - dashed lines $10 < E_e < 25$ keV - dotted lines $25 < E_e < 50$ keV - solid lines $E_e > 50$ keV - dash-dot lines for the acceleration in the coarsely (red lines) and finely (blue lines) resolved magnetic fields.

5. Conclusions and Discussion

5.1. Conclusions

In contrast to acceleration in direct current (DC) parallel electric fields which in MHD simulations depends on the choice of the resistivity in the Ohms law, we concentrate on the acceleration due to magnetic gradient and curvature drift effects in the cascading reconnection current sheet. We found that both trapped in the magnetic islands and precipitating electrons can be accelerated by the perpendicular magnetic gradients and curvatures. Trapped energetic electrons contribute to the formation of bright spots along the current sheet trailing CMEs or eruptive filaments) as well as the flare loop-top HXR radiation by their Bremsstrahlung. Precipitating electrons, on the other hand, cause ribbons of UV and EUV brightening in the solar chromosphere.

Whether an electron becomes trapped or precipitating depends on the initial conditions (e.g., for precipitation, an electron should have a position around X-points, velocity $> 2 v_{th}$ and pitch angle $\neq 90^\circ$). Trapped electrons are energized mainly in the magnetic islands in the coarse magnetic fields, while in the better resolved magnetic fields, the strongest trapped electron acceleration takes place close to the X-points due to there finely resolved larger magnetic curvatures and gradients in the smaller-scale magnetic fields. Both trapped and precipitating electrons are accelerated or decelerated in dependence on their initial positions and pitch angles. The electron final kinetic energy strength depends on the initial electron energy - larger initial energies cause stronger accelerations. As well as every kind of electron can get more energization if the smaller-scale magnetic structures, obtained by higher resolution MHD simulations, are taken into account. Also because of these smaller-scale structures, energization of more accelerated trapped electrons are mainly in the parallel direction in the finer magnetic fields. Other (less accelerated trapped and precipitating) electrons mainly gain energies in the perpendicular direction. Due to the asymmetry in the magnetic curvature drift acceleration term around the center of 2.5D current sheet, the larger magnetic curvatures in the better resolved magnetic structures cause stronger non-symmetric accelerations around initial pitch angle 90° of trapped and precipitating electrons. On the contrary, in the coarsely resolved magnetic fields both trapped and precipitating electron acceleration are close to symmetric around 90° .

With the better resolved small-scale magnetic structures, the maximum energy gain of trapped electrons can be up to 421 keV. This already suffices to explain the observed loop-top HXR radiations. Under the thin target model together with a simple Bethe-Heitler formula for the cross section of Bremsstrahlung and an initial distributions function $\propto E_0^0$ (or constant) and $\propto E_0^{-3}$, the HXR spectral indices of trapped electrons can be as hard as ~ 5 in the better resolved magnetic fields. This is already hard enough to explain the observed HXR spectra in medium solar flares. For initial Maxwell-Boltzmann distributions for $T = 10^6$ K, the HXR spectra provide, however, just a slight enhancement of the high energy tail.

In the chromospheric ribbon-shape locations of precipitating electrons, electrons starting lower in the solar atmosphere precipitate closer to the PIL. The weak parallel acceleration of precipitating electron leads electrons with initial pitch angles $< 90^\circ$ precipitate to one side of the PIL, while ones with initial pitch angles $> 90^\circ$ go to the other side of the PIL. Generally, there is a anti-symmetrical geometry of precipitating electron locations in chromosphere around the PIL. While because of the stronger accelerations of electrons with initial pitch angles $> 90^\circ$, more energetic electrons are located in one side of the PIL only with the better resolved smaller-scale magnetic structures.

5.2. Discussion

Solar flare observations imply that a large number of energetic electrons should precipitate into the solar chromosphere where they cause observable radiations. Our calculations have shown that only 12% electrons can precipitate within $10 t_0$. While the whole current sheet evolution is as long as $520 t_0$. Depending on the magnetic field evolutions (see panels of Fig.1), lower magnetic islands ($x < 70 L_0$) in Fig.10) will merge into one magnetic loop (see right panel of Fig.1) eventually. So in the end, the electrons previously trapped in the lower magnetic islands can later also precipitate to the chromosphere. Taking into account this merging effects, more than 63% electrons will finally reach the chromosphere. As well as when the space scale collapses to the kinetic one, the guiding center approximation will be not valid any more. Particle motion will become chaotic due to nonlinear resonances between particle bounce motion and gyration. With the transition to chaos, Buechner & Zelenyi 1989 found that trapped nonadiabatic charged particles can escape due to chaotic pitch angle scattering effects. Furthermore in this study during $10 t_0$, the background electromagnetic fields are constant, so the time effects on electron acceleration are neglected. With the evolutions of the electromagnetic fields, maybe some trapped electrons become precipitating ones. As a result, even more electrons will precipitate.

Our study can explain the observed medium and small solar flare loop-top HXR spectra and EUV-ribbons just based on magnetic gradient and curvature effects in magnetic islands without ad hoc postulated "anomalous" resistivity. Precipitating electrons in our results, however, cannot explain the HXR spectral indices in the foot-points of solar flares which can be as hard as 1.5 in large solar flares. Precipitating electrons also could reach the energies necessary to explain

the observed HXR spectra bases on magnetic gradient and curvature effects if more and smaller magnetic field structures are formed by cascading magnetic reconnection.

Appendix A: Validation of the accuracy by using the conservation of the Second Adiabatic Invariant

The conservation of the second adiabatic invariant (Northrop 1963) of trapped electrons can be used to validate the accuracy of the numerical scheme solving Eqs.(11) to (14):

$$J_{\parallel} = m \int_b^a v_{\parallel} dl \cong \text{constant} \quad (\text{A.1})$$

In Eq.(A.1), the integral is taken along the particle guiding center trajectory between the mirror points 'a' and 'b'. Fig.A.1 shows an example electron with conserved J_{\parallel} .

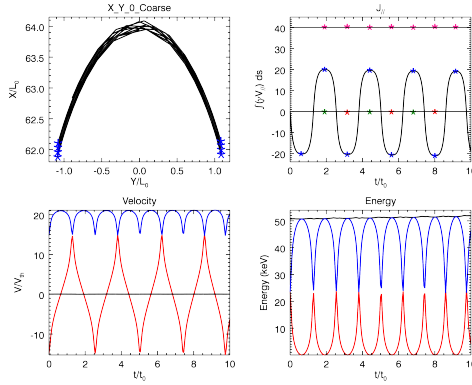


Fig. A.1. Characteristic electron orbit indicating the conservation of the second adiabatic invariant. The *upper left* panel shows the XY-projection of the trajectory and the *blue ** points in this panel corresponding to the mirror points. The *upper right* panel shows J_{\parallel} values along the trajectory and its *red, green and deep pink ** points show absolute changes of J_{\parallel} during half-period (deep pink * points) or one-period (red and green * points). Three kinds of velocity (perpendicular gyration velocity - *blue* line, parallel velocity - *red* line and drift velocity - *dark* line) and energy (perpendicular gyration energy - *blue* line, parallel energy - *red* line and total kinetic energy - *dark* line) are separately shown in the *bottom left* and *right* panel.

The upper left panel of Fig.A.1 depicts the XY-projection of the electron trajectory. Every blue asterisks in the upper right panel of Fig.A.1 corresponds to a mirror point. Note that in the definition of the second adiabatic invariant J_{\parallel} (Eq.(A.1)), $dl > 0$ when the particle is moving forward and $dl < 0$ when it is moving backward. For a convenience here we do not change the sign of 'dl' when calculating the values of J_{\parallel} along the electron trajectory. One easily obtains not only the constant J_{\parallel} over half-period (deep pink '*' points) but also the vanishing J_{\parallel} over a whole bounce period (red and green '*' points) as one can see in the upper right panel of Fig.A.1. A comparison of parallel and perpendicular gyration velocities with the drift velocities along the electron trajectory (bottom left panel of Fig.A.1) illustrates the validation of the second adiabatic invariant. The bottom right panel of Fig.A.1 indicates that the total kinetic energy is exchanged between the parallel and the perpendicular directed motion.

Acknowledgements. This work was supported by the German-Chinese center of collaboration by the Max-Planck-Institute for Solar System Research, by the Max-Planck-Princeton Center for Plasma Physics and by the program of 2011CB811402 from MSTC and grants of 11233008, 11427803 from NNSFC. Lots of thanks to all members (e.g., Jan Skala, Patricio Munoz, Fabien Widmer) of the Theory and Simulation of Solar System Plasmas (TSSSP) group and Thomas Wiegelmann

in the Max Planck Institute for Solar System Research (MPS), Germany for their useful and fruitful discussions and suggestions.

References

- Aschwanden, M. J. 2002, *Space Sci. Rev.*, 101, 1
- Bárta, M., Büchner, J., & Karlický, M. 2010, *Advances in Space Research*, 45, 10
- Bárta, M., Büchner, J., Karlický, M., & Skála, J. 2011, *ApJ*, 737, 24
- Benz, A. O. 2008, *Living Reviews in Solar Physics*, 5, 1
- Bethe, H. & Heitler, W. 1934, *Royal Society of London Proceedings Series A*, 146, 83
- Birn, J. & Priest, E. R. 2007, *Reconnection of Magnetic Fields*
- Brown, J. C. 1971, *Sol. Phys.*, 18, 489
- Büchner, J. & Elkina, N. 2005, *Space Sci. Rev.*, 121, 237
- Büchner, J. & Elkina, N. 2006, *Physics of Plasmas*, 13, 082304
- Buechner, J. & Zelenyi, L. M. 1989, *J. Geophys. Res.*, 94, 11821
- Burkhart, G. R., Drake, J. F., & Chen, J. 1990, *J. Geophys. Res.*, 95, 18833
- Carrington, R. C. 1859, *MNRAS*, 20, 13
- Ciaravella, A., Raymond, J. C., Li, J., et al. 2002, *ApJ*, 575, 1116
- Datlowe, D. W. & Lin, R. P. 1973, *Sol. Phys.*, 32, 459
- Fletcher, L., Dennis, B. R., Hudson, H. S., et al. 2011, *Space Sci. Rev.*, 159, 19
- Gordovskyy, M., Browning, P. K., & Vekstein, G. E. 2010a, *A&A*, 519, A21
- Gordovskyy, M., Browning, P. K., & Vekstein, G. E. 2010b, *ApJ*, 720, 1603
- Guo, J.-N., Büchner, J., Otto, A., et al. 2010, *A&A*, 513, A73
- Hodgson, R. 1859, *MNRAS*, 20, 15
- Holman, G. D., Aschwanden, M. J., Aurass, H., et al. 2011, *Space Sci. Rev.*, 159, 107
- Hoshino, M., Nishida, A., Yamamoto, T., & Kokubun, S. 1994, *Geophys. Res. Lett.*, 21, 2935
- Karlický, M. 2004, *A&A*, 417, 325
- Karlický, M. & Bárta, M. 2006, *ApJ*, 647, 1472
- Karlický, M. & Bárta, M. 2008, *Sol. Phys.*, 247, 335
- Karlický, M., Bárta, M., & Nickeler, D. 2012, *A&A*, 541, A86
- Karlický, M. & Kosugi, T. 2004, *A&A*, 419, 1159
- Ko, Y.-K., Raymond, J. C., Lin, J., et al. 2003, *ApJ*, 594, 1068
- Krucker, S., Battaglia, M., Cargill, P. J., et al. 2008, *A&A Rev.*, 16, 155
- Li, Y. & Lin, J. 2012, *Sol. Phys.*, 279, 91
- Lin, J. & Forbes, T. G. 2000, *J. Geophys. Res.*, 105, 2375
- Lin, R. P. & Hudson, H. S. 1976, *Sol. Phys.*, 50, 153
- Loureiro, N. F., Schekochihin, A. A., & Cowley, S. C. 2007, *Physics of Plasmas*, 14, 100703
- Martens, P. C. H. & Young, A. 1990, *ApJS*, 73, 333
- Masuda, S., Kosugi, T., Hara, H., Tsuneta, S., & Ogawara, Y. 1994, *Nature*, 371, 495
- Miller, J. A., Cargill, P. J., Emslie, A. G., et al. 1997, *J. Geophys. Res.*, 102, 14631
- Northrop, T. G. 1963, *The Adiabatic Motion of Charged Particles*
- Priest, E. R. 1984, *Solar magneto-hydrodynamics*
- Priest, E. R. & Forbes, T. G. 2002, *A&A Rev.*, 10, 313
- Priest, E. R. & Titov, V. S. 1996, *Royal Society of London Philosophical Transactions Series A*, 354, 2951
- Savage, S. L., McKenzie, D. E., Reeves, K. K., Forbes, T. G., & Longcope, D. W. 2010, *ApJ*, 722, 329
- Shibata, K. & Tanuma, S. 2001, *Earth, Planets, and Space*, 53, 473
- Silin, I., Büchner, J., & Vaivads, A. 2005, *Physics of Plasmas*, 12, 062902
- Tandberg-Hanssen, E. & Emslie, A. G. 1988, *The physics of solar flares*

- Uzdensky, D. A., Loureiro, N. F., & Schekochihin, A. A. 2010, *Physical Review Letters*, 105, 235002
- Vekstein, G. E. & Browning, P. K. 1997, *Physics of Plasmas*, 4, 2261
- Vlahos, L. & Cargill, P. 2009, *Turbulence in Space Plasmas*
- Wood, P. & Neukirch, T. 2005, *Sol. Phys.*, 226, 73
- Zharkova, V. V., Arzner, K., Benz, A. O., et al. 2011, *Space Sci. Rev.*, 159, 357
- Zharkova, V. V. & Gordovskyy, M. 2004, *ApJ*, 604, 884
- Zharkova, V. V. & Gordovskyy, M. 2005a, *MNRAS*, 356, 1107
- Zharkova, V. V. & Gordovskyy, M. 2005b, *Space Sci. Rev.*, 121, 165

List of Objects